Automatically interpreting all faults, unconformities, and horizons from 3D seismic images

Xinming Wu[1] and Dave Hale[1]

Abstract

Extracting fault, unconformity, and horizon surfaces from a seismic image is useful for interpretation of geologic structures and stratigraphic features. Although others automate the extraction of each type of these surfaces to some extent, it is difficult to automatically interpret a seismic image with all three types of surfaces because they could intersect with each other. For example, horizons can be especially difficult to extract from a seismic image complicated by faults and unconformities because a horizon surface can be dislocated at faults and terminated at unconformities. We have proposed a processing procedure to automatically extract all the faults, unconformities, and horizon surfaces from a 3D seismic image. In our processing, we first extracted fault surfaces, estimated fault slips, and undid the faulting in the seismic image. Then, we extracted unconformities from the unfaulted image with continuous reflectors across faults. Finally, we used the unconformities as constraints for image flattening and horizon extraction. Most of the processing was image processing or array processing and was achieved by efficiently solving partial differential equations. We used a 3D real example with faults and unconformities to demonstrate the entire image processing.

Introduction

From a 3D seismic image, as shown in Figure 1, one can extract geologic surfaces such as faults, unconformities, and horizons. Faults and horizons are important for seismic structural interpretation because they provide structural maps of the subsurfaces. Horizons and unconformities are important for seismic stratigraphic interpretation because together they construct a chronostratigraphic framework. All these geologic surfaces can be useful for seismic lithology interpretation because they can provide geologically reasonable control for extending a lithology interpretation away from wells. Therefore, extracting these surfaces is a critical part of seismic interpretation.

Fault interpretation

Automatic interpretation of faults from a seismic image often involves the following four steps: (1) Fault attributes such as semblance (Marfurt et al., 1998), coherency (Marfurt et al., 1999), variance (Van Bemmel and Pepper, 2000; Randen et al., 2001), and fault likelihood (Hale, 2013b) are computed from a seismic image to highlight fault positions. (2) Fault surfaces are extracted from these computed fault images using various methods (Pedersen et al., 2002, 2003; Gibson et al., 2005; Hale, 2013b (3) From extracted fault surfaces, fault slips are estimated by correlating picked seismic horizons (Admasu, 2008) or all seismic reflectors (Hale,

2013b) on opposite sides of fault surfaces. (4) Computed fault positions and fault slips are finally used to undo the faulting in the seismic image (Wei et al., 2005; Wei, 2009; Luo and Hale, 2013).

In most methods for fault extraction, the problem of extracting intersecting faults is not well addressed, and the extracted fault surfaces are often represented by triangle or quad meshes, which are often more complex than necessary for subsequent processing. Wu and Hale (2015a) propose to use a simpler linked data structure to represent a fault surface, to extract multiple intersecting fault surfaces without holes at intersection, and to accurately estimate fault slips. Most unfaulting methods (Wei et al., 2005; Wei, 2009; Luo and Hale, 2013) assume that fault geometries need not change to undo the faulting in a seismic image. This assumption makes the unfaulting processing easier, but often results in unnecessary distortions when unfaulting seismic images with multiple faults and, especially, intersecting faults. Wu et al. (2015) propose two methods to simultaneously move fault blocks and faults themselves to undo faulting in a seismic image with minimal distortion.

Unconformity interpretation

To obtain complete unconformities from a seismic image, we want to extract the angular unconformities with reflector terminations and the corresponding parallel unconformity or correlative conformity with

---

conformable reflectors. Most automatic methods can detect only angular unconformities by computing attributes such as seismic coherence (Bahorich and Farmer, 1995) and seismic reflector convergence or divergence (Barnes et al., 2000; Hoek et al., 2010) to highlight areas of reflector terminations. Ringdal (2012) proposes a 2D flow-based method to compute unconformity probability that can highlight termination areas and parallel unconformity or correlative conformity. However, the flow field used in this method is difficult to represent in 3D. For 3D seismic images, this method processes inline and crossline slices separately to compute an unconformity probability volume.

Wu and Hale (2015b) propose 3D image processing methods to (1) compute an unconformity likelihood image that highlights the termination areas and the corresponding parallel unconformities or correlative conformities, (2) extract unconformity surfaces from the unconformity likelihood image, and, finally, (3) use the unconformity surfaces as constraints to accurately estimate seismic normal vectors at unconformities and to compute a flattened image with vertical gaps corresponding to the unconformities.

Horizon interpretation

Automatic seismic image flattening (Stark, 2005; Lomask et al., 2006; Fomel, 2010; Parks, 2010; Wu and Zhong, 2012; Luo and Hale, 2013) is a volume process method to identify all horizons in a seismic image by computing a mapping that transforms the seismic image from the original space into the flattened space. This mapping can be used to extract any number of horizons from the seismic image. However, these methods are unable to match horizons across faults unless additional information such as fault slips (Luo and Hale, 2013) and control points across faults (Wu and Hale, 2015c) are provided. Also, these methods cannot adequately deal with horizons terminated at unconformities unless the unconformity surfaces are provided (Wu and Zhong, 2012; Wu and Hale, 2015b).
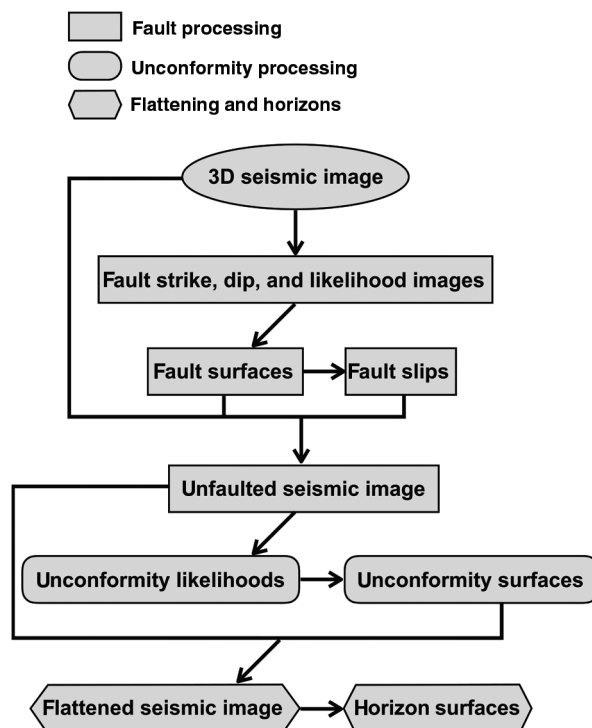
This paper

We present a feasible procedure, as shown in Figure 2, to automatically interpret a complicated seismic image with faults and unconformities, as shown in Figure 1. It is complicated because many intersecting faults are apparent in the seismic image, unconformities, and horizons are dislocated by faults, and many horizons are also terminated at unconformities.

To automatically interpret such a seismic image and obtain all faults, unconformities, and horizon surfaces, we apply the following procedure (Figure 2): (1) We first apply the fault-processing methods proposed by Wu and Hale (2015a) to compute fault surfaces and slips from the seismic image and use them to undo the faulting in the seismic image. (2) We then apply the unconformity processing methods proposed by Wu and Hale (2015b) to extract unconformities from the unfaulted image with continuous seismic reflectors across faults and use them as constraints to more accurately estimate seismic normal vectors at unconformities with multioriented seismic reflectors. (3) Next, we use the estimated normal vectors, and use the unconformities as constraints, for a flattening method to compute an unfaulted and flattened image with vertical gaps corresponding to the unconformities. After unfaulting and flattening, one can easily compute horizon surfaces by first extracting horizontal slices in the unfaulted and flattened space and then mapping these slices back to the original space.

Figure 1. A 3D real seismic image complicated by faults (red arrows) and unconformities (yellow arrows).

Figure 2. Our processing procedure to automatically interpret a complicated seismic image with faults and unconformities as shown in Figure 1.

Fault processing

Because unconformities and horizons are discontinuous at faults, as shown in Figure 1, our first step is fault processing to extract fault surfaces, compute fault slips, and undo the faulting in the seismic image, so that seismic reflectors are more continuous across faults.

Fault images and surfaces

We assume faults appear as discontinuities that are locally planar in 3D seismic images and linear in 2D slices like those shown in Figures 1 and 3. The key point of this assumption is that when looking for faults, we are not simply looking for discontinuities. Rather, we are looking for discontinuities that are locally planar. With this assumption, we use the method proposed by Hale (2013b) to compute fault likelihood, a measure of locally planar discontinuity, while at the same time estimating fault strike and dip. The fault likelihood image indicates where faults might exist (Figure 3a), whereas the strike and dip images indicate their orientations.

In computing these fault images, this method scans over a range of possible combinations of strike and dip to find the one orientation that maximizes the fault likelihood for each image sample (Hale, 2013b). The maximum fault likelihood for each image sample is recorded in the fault likelihood image as shown in Figure 3a, and the strike and dip angles that yield the maximum likelihood are recorded in the fault strike and dip images, which are not shown here. In the fault likelihood image in Figure 3a, we expect relatively high values in areas where faults might exist.

However, we do not expect faults to be as thick as the features apparent in the fault likelihood image in Figure 3a. Therefore, we keep only the values on the ridges of the fault likelihoods, and set values elsewhere to be zero, to obtain a thinned fault likelihood image shown in Figure 3b. We also keep strike and dip angles for only the samples with nonzero values in Figure 3b, to obtain the corresponding thinned fault strike and dip images, which are not shown here. These thinned fault images have nonzero values only for samples that might be on faults.

As discussed by Wu and Hale (2015a), because most samples in the thinned fault images of fault likelihood, strike, and dip are zero, we can display nonzero samples of the three images, all at once, as fault samples shown in Figure 4a. Each fault sample is displayed as a colored square. The color of each square denotes fault likelihood, whereas the orientation of each square represents fault strike and dip. Fault samples exist only at positions where thinned fault likelihoods are nonzero, and each fault sample corresponds to one and only one image sample. Therefore, these fault samples contain exactly the same information represented in all three thinned fault images.

Most fault samples, especially those with high fault likelihoods, are aligned approximate planes, consistent with locally planar fault surfaces. Some misaligned fault samples, often with low fault likelihoods, are also observed in Figure 4a. However, these misaligned samples cannot be linked together to form locally planar fault surfaces of significant sizes.

With the fault samples shown in Figure 4a, we apply the method described in Wu and Hale (2015a) to extract fault surfaces (Figure 4b) by linking nearby fault samples with similar fault likelihoods, strikes, and dips. Each fault surface is represented by a set of linked fault samples and not a mesh of triangles or quadrilaterals. The samples on a surface are linked above and below in the fault dip direction and left and right in the strike direction. These links enable us to iterate among seismic image samples adjacent to a fault, in dip and strike directions, as we estimate fault slips. The sets of linked fault samples can be displayed as opaque fault surfaces, as in Figure 4b, by simply increasing the size of each square so that they overlap and appear to form continuous surfaces.

However, these surfaces are really just sets of linked fault samples located within the sampling grid of the seismic image; therefore, these surfaces colored by fault likelihoods can also be easily displayed as a 3D fault likelihood image (with nonzero values only at faults) overlaid with the seismic image in Figure 5a. Compared to the thinned fault likelihood image in Figure 3b, spurious fault samples have been removed because they cannot be linked to form fault surfaces with significant sizes.
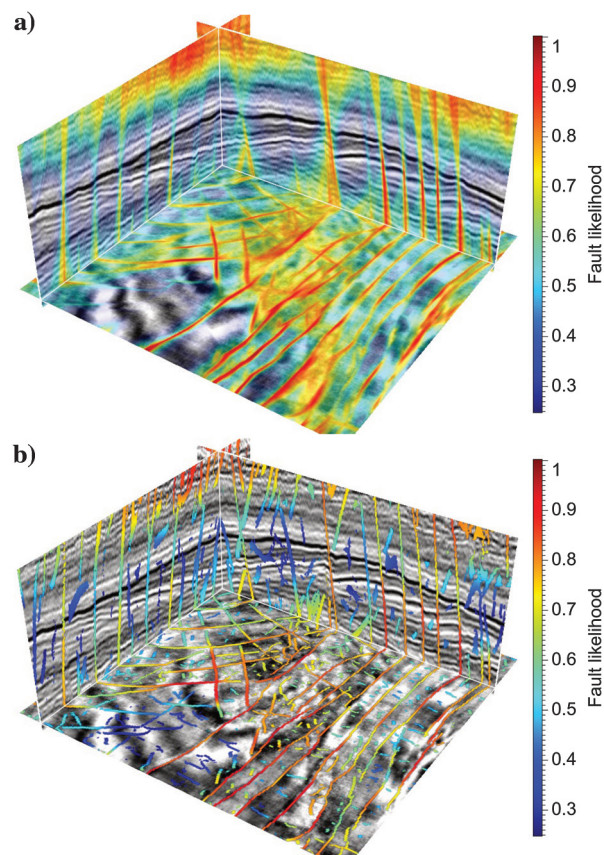
Figure 3. Fault image of likelihoods (a) before and (b) after thinning. The fault likelihoods in panel (a) are displayed in translucent colors.

We use the fault likelihood image (Figure 5a) to constrain a structure-oriented filter (Fehmers and Höcker, 2003; Hale, 2009) so that it smoothes along structures, but not across faults, to obtain the smoothed seismic image shown in Figure 5b. We then use this smoothed image, instead of the original seismic image, to estimate fault slips. This smoothing does what seismic interpreters do visually when estimating fault slips. We never estimate fault slips using only image samples adjacent to faults; instead, we look at entire fault blocks. This smoothing brings seismic amplitudes from within each fault block up to, but not across, the faults.

Fault slips and unfaulting

Fault slip is a vector representing displacement of the hanging wall of a fault surface relative to the footwall. In practice, we only estimate dip-slip vectors and relative displacements up or down along the dip of a fault because they are usually more significant than strike-slip displacements in seismic images. Moreover, dip-slip vectors are usually more perpendicular to seismic reflectors, and therefore easier to estimate by cor-

relating seismic reflectors across faults, than are strike-slip displacements.

As discussed by Wu and Hale (2015a), to estimate fault dip slip, we first estimate fault throw, the vertical component of dip slip, using the dynamic warping method (Hale, 2013a). Recall that each fault surface in Figure 4b is a set of linked fault samples. The links among fault samples enable us to conveniently iterate on a fault surface and compute differences between seismic amplitudes on opposite sides of the fault. These amplitude differences are computed for every sample on the fault, for a range of shifts that correspond to different fault throws. The fault throws computed by dynamic warping are shifts that minimize these seismic amplitude differences, subject to constraints that the shifts must vary smoothly along the fault surface.

Knowing the fault surface with linked fault samples and the computed fault throws, we can walk up or down the fault in the dip direction to compute horizontal components of the dip-slip vector. For each fault sample, the fault throw tells us how far upward or downward along the dip direction we must iterate within the linked fault samples to determine the horizontal inline and crossline components of the dip-slip vector. It is usually difficult to visualize dip-slip vectors in displays of numerous faults.
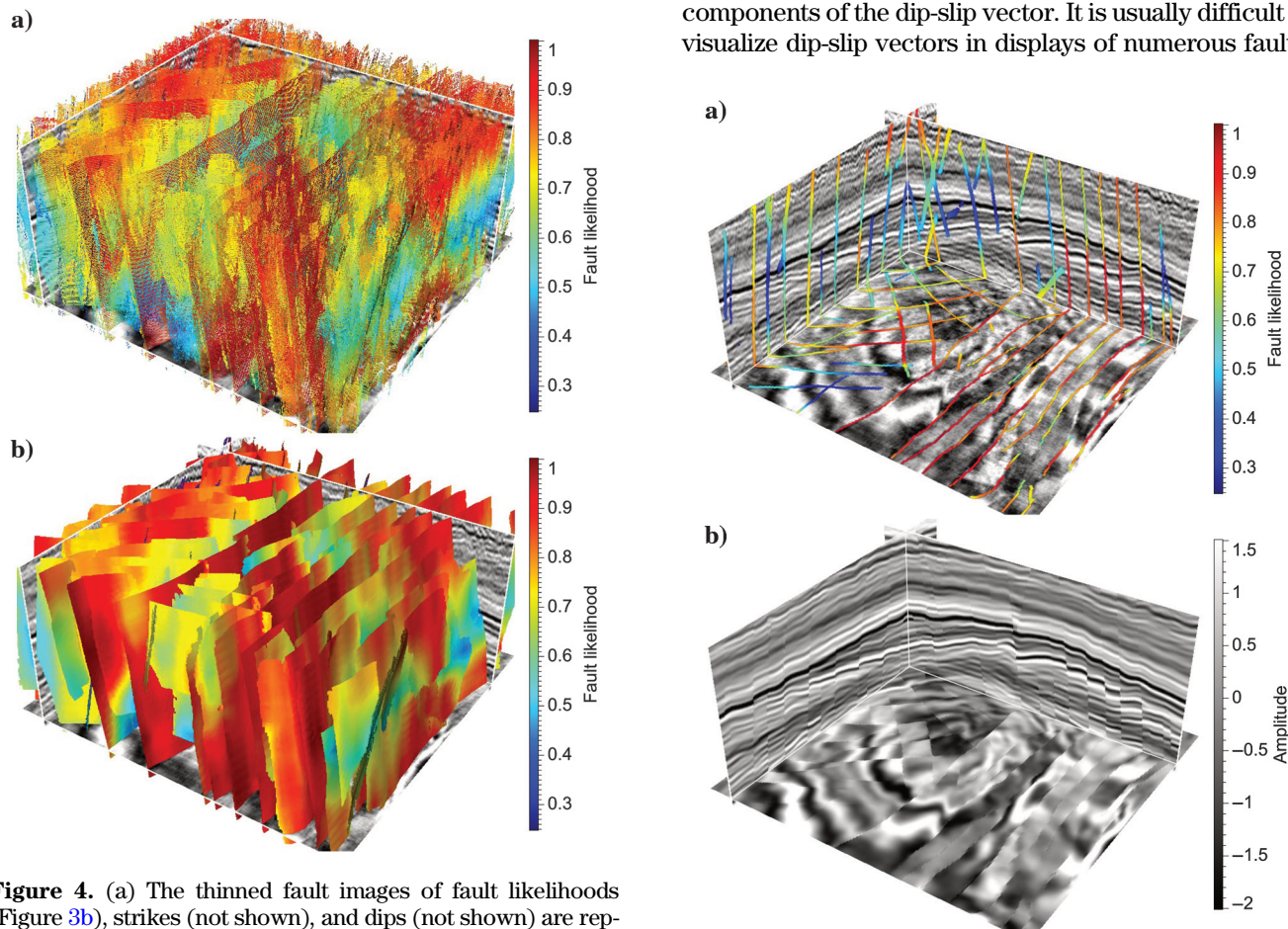
Figure 4. (a) The thinned fault images of fault likelihoods (Figure 3b), strikes (not shown), and dips (not shown) are represented, all at once, as fault samples that are displayed as small squares. Each square is colored by fault likelihood and oriented by fault strike and dip. Links are then built among consistent fault samples, and each set of linked fault samples represents a fault surface that appears opaque in panel (b), where fault samples are displayed as larger overlapping squares.

Figure 5. The fault surfaces in Figure 4b are displayed as a fault likelihood image with mostly zeros in panel (a). This fault image is used to constrain a structure-oriented smoothing filter so that it smoothes along structures, but not across faults, to obtain a smoothed seismic image in panel (b).

Therefore, although estimating all three components of dip-slip vectors, we display in color only the vertical components (or fault throws) on the fault surfaces in Figure 6a. Because the vertical axis of the seismic image is time (not depth), fault throws are here measured in milliseconds, but this method works equivalently for seismic images measured in depth. These surfaces colored by fault throws in Figure 6a can also be displayed as a 3D fault throw image (with nonzero values only at faults) overlaid with the seismic image slices shown in Figure 6b. We observe that fault throws estimated for each fault surface vary smoothly. Also fault throws are non-negative for all fault surfaces, which indicates that the faults shown here are normal faults.

As shown in Figure 6, fault slips are estimated on fault surfaces and tell us how to correlate only the samples alongside faults. However, to undo the faulting in a seismic image without distortions, we cannot simply shift just the samples alongside the faults. Instead, we must shift all samples in the image and move entire fault blocks and even faults themselves, as discussed by Wu et al. (2015). Most unfaulting methods (Wei et al., 2005; Luo and Hale, 2013) assume that the geometry of faults does not change and move only fault blocks when unfaulting a seismic image. As discussed by Wu et al.

(2015), this assumption usually results in unnecessary distortions when unfaulting a seismic image with multiple faults and, especially, intersecting faults like those on the left of the horizontal slice in Figure 6b.

Here, we use the method proposed by Wu et al. (2015) to undo the faulting in the seismic image shown in Figure 6b. In this method, unfaulting shifts $s_k(\mathbf{x})$ are computed in the original space ($\mathbf{x} = (x_1, x_2, x_3)$) by simultaneously solving the following partial differential equations and unfaulting equations:

$$\omega(\mathbf{x})\nabla s_k(\mathbf{x}) \approx \mathbf{0}$$
$$\beta c(\mathbf{x}_a)(s_k(\mathbf{x}_b) - s_k(\mathbf{x}_a)) \approx \beta c(\mathbf{x}_a)t_k(\mathbf{x}_a), \qquad (1)$$
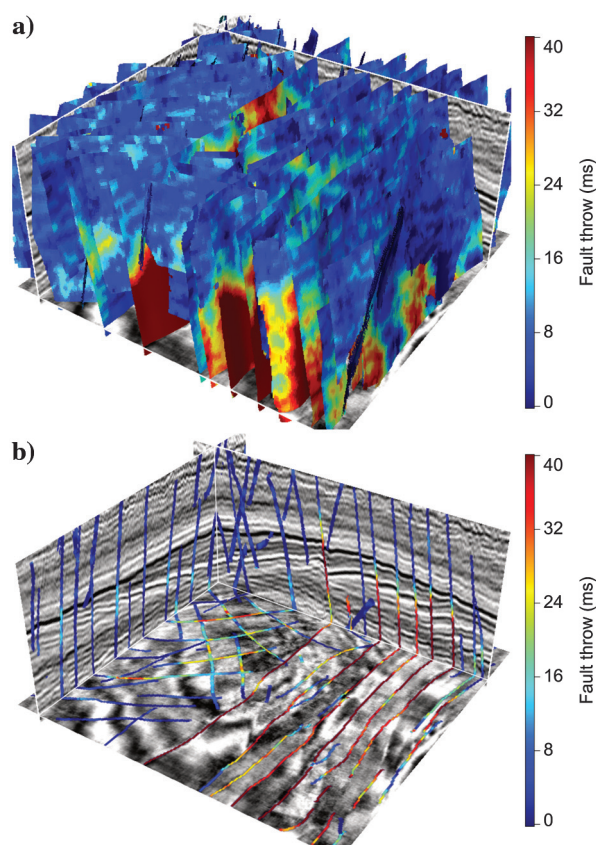
Figure 6. (a) All three components of fault dip slips are estimated on fault surfaces, but only fault throws and the vertical components of slips are displayed in color on fault surfaces. These colored surfaces can be displayed as (b) a 3D fault throw image (with mostly zeros) overlaid with the seismic image.
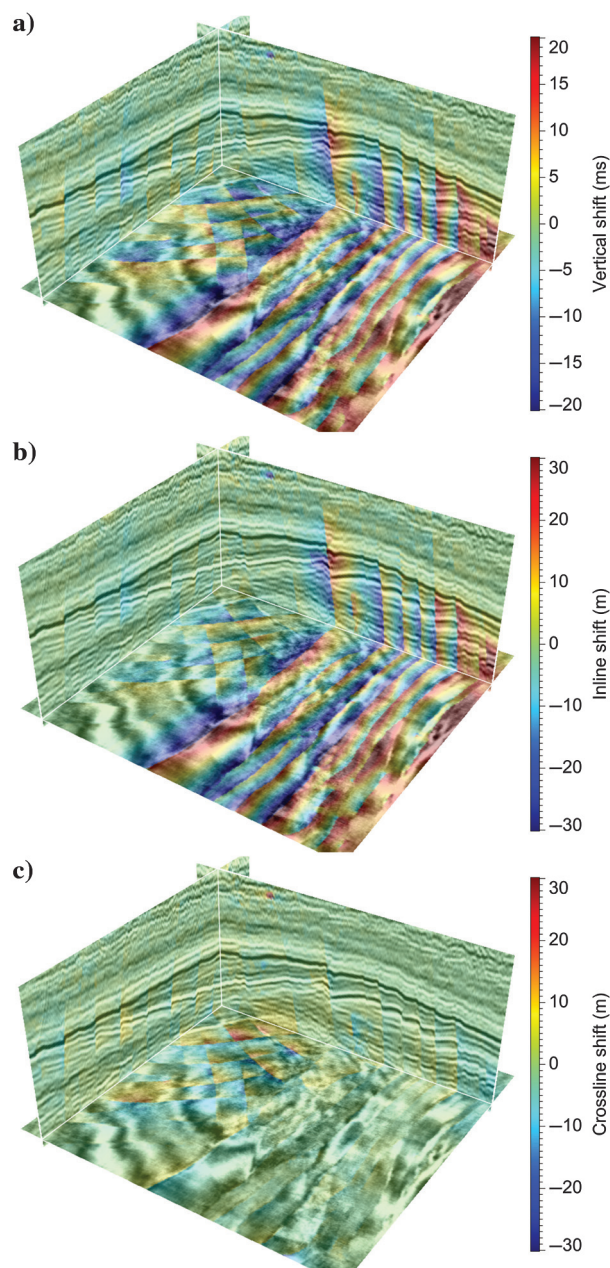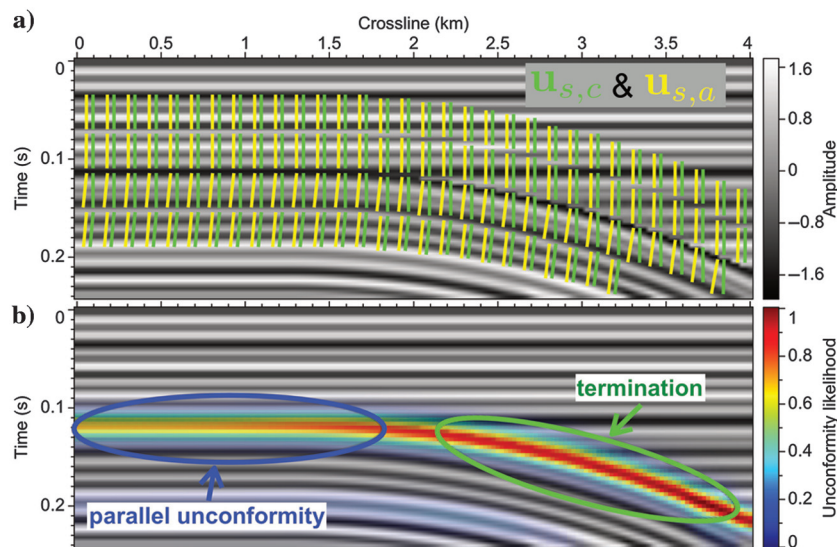

Figure 7. (a) Unfaulting shifts in vertical, (b) inline, and (c) crossline directions, respectively.
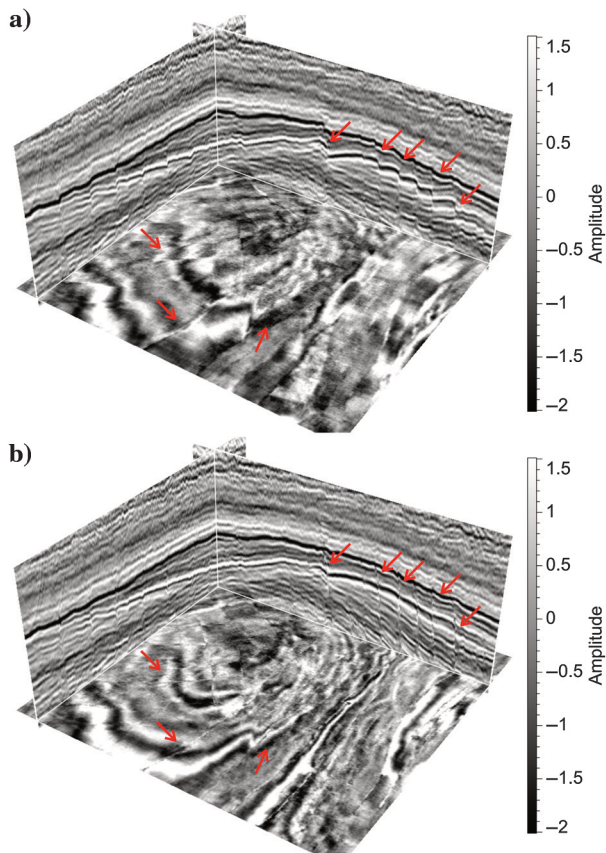
Figure 8. A seismic image (a) before and (b) after unfaulting. Seismic reflectors are more continuous across faults after unfaulting as highlighted by the red arrows.

where ∇ represents the gradient operator and $s_k(\mathbf{x})$ ($k = 1, 2, 3$) represent the three components of vector shifts for all samples in an image. Here, $\omega(\mathbf{x})$ is a weighting function that is zero at image samples adjacent to faults and is one elsewhere. Therefore, this equation is actually defined at all image samples except those adjacent to faults. This equation means that we expect unfaulting shifts to vary slowly and continuously at samples away from faults; $t_k(\mathbf{x})$ ($k = 1, 2, 3$) represent the three components of fault slip vectors estimated on faults; $\mathbf{x}_a$ and $\mathbf{x}_b$ represent samples adjacent to the faults from footwall and hanging wall, respectively. Therefore, this unfaulting equation is defined only for samples adjacent to their faults using the estimated fault positions and fault slip vectors; $c(\mathbf{x})$ is a measure of the quality of the estimated slips, and here, we use the fault likelihoods that are already computed on faults; β is a constant number used to balance the partial differential equations and the unfaulting equations.

By solving these two different types of equations simultaneously, we obtain unfaulting shifts $s_k(\mathbf{x})$ for all samples in the original space ($\mathbf{x} = (x_1, x_2, x_3)$). These shifts $s_k(\mathbf{x})$ can be easily converted into the unfaulted space ($\mathbf{w} = (w_1, w_2, w_3)$) to obtain $s_k(\mathbf{w})$ as discussed in Wu et al. (2015) because the mapping between the original space and unfaulted space is reversible. Figure 7 shows all three components of unfaulting shifts $s_k(\mathbf{w})$ overlaid with the seismic image. We observe that each component of the shifts is continuous everywhere except at faults. These vector shifts simultaneously move footwalls and hanging walls, and even faults themselves to undo the faulting in the seismic image (Figure 8a) to compute an unfaulted image shown in Figure 8b. In this unfaulted image, all seismic reflectors are well aligned across faults and no distortion is observed.

Unconformity processing

From an unfaulted image (Figure 8b) with more continuous reflectors across faults, interpretation of seismic horizons and unconformities becomes more straightforward. Before extracting seismic horizons, we want to first interpret unconformities because horizons might be terminated at unconformities and the interpreted unconformities can serve as constraints for manual and automatic horizon extractions.

To obtain complete unconformities from a seismic image, we want to extract angular unconformities with reflector terminations and the corresponding parallel unconformity or correlative conformity with conformable reflectors. Most automatic methods (Bahorich and Farmer, 1995; Barnes et al., 2000; Smythe et al., 2004; Hoek et al., 2010) can detect only angular unconformities. Here, we use

Figure 9. Two seismic normal vector fields (a) $\mathbf{u}_{s,c}$ (green) and $\mathbf{u}_{s,a}$ (yellow) are computed from structure tensors that are constructed with vertically causal and anticausal smoothing filters, respectively. These two vector fields are different near the unconformity, and (b) unconformity likelihood is an attribute that evaluate the differences of the two vector fields.

the method proposed by Wu and Hale (2015b) to compute an unconformity likelihood image that highlights the termination areas and the corresponding parallel unconformities, as shown in Figures 9b and 10a.

As discussed by Wu and Hale (2015b), the unconformity likelihood is defined as an attribute that evaluates the differences between two seismic normal vector fields estimated from a same seismic image. These two vector fields correspond to the largest eigenvectors of the two structure-tensor fields $\mathbf{T}_{s,c}$ and $\mathbf{T}_{s,a}$ constructed from the same seismic image but with different smoothing filters:

$$\mathbf{T}_{s,c} = \begin{bmatrix} \langle\langle g_1 g_1 \rangle_s \rangle_c & \langle\langle g_1 g_2 \rangle_s \rangle_c \\ \langle\langle g_1 g_2 \rangle_s \rangle_c & \langle\langle g_2 g_2 \rangle_s \rangle_c \end{bmatrix} \quad (2)$$

and

$$\mathbf{T}_{s,a} = \begin{bmatrix} \langle\langle g_1 g_1 \rangle_s \rangle_a & \langle\langle g_1 g_2 \rangle_s \rangle_a \\ \langle\langle g_1 g_2 \rangle_s \rangle_a & \langle\langle g_2 g_2 \rangle_s \rangle_a \end{bmatrix}, \quad (3)$$

where g_1 and g_2 are the first derivatives of the seismic image in vertical and horizontal directions, respectively. The first structure-tensor field $\mathbf{T}_{s,c}$ is constructed by first applying a laterally structure-oriented smoothing filter $\langle\cdot\rangle_s$ and then a vertical causal filter $\langle\cdot\rangle_c$ to each element of the tensor. The other one $\mathbf{T}_{s,a}$ is constructed by applying the same laterally structure-oriented smoothing filter but a vertical anticausal filter $\langle\cdot\rangle_a$.

Near the termination area of an unconformity, the reflector structures above and below the unconformity must be different. Therefore, the vertical causal filter, which computes locally averaged structures from above the unconformity, yields a structure-tensor field that is different from the one constructed with the vertical anticausal filter, which computes locally averaged structures from below. The lateral structure-oriented
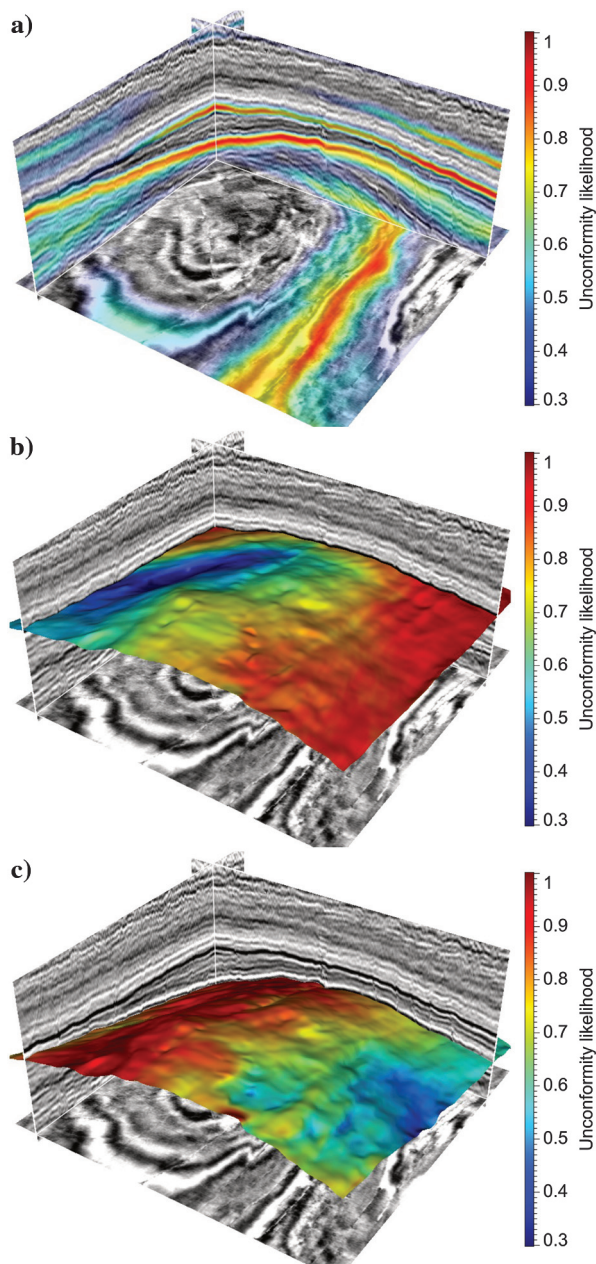

Figure 10. From the unfaulted image with continuous reflectors across faults, (a) an unconformity likelihood image is first computed, and then (b) and (c) unconformity surfaces are extracted on the ridges of the unconformity likelihoods.
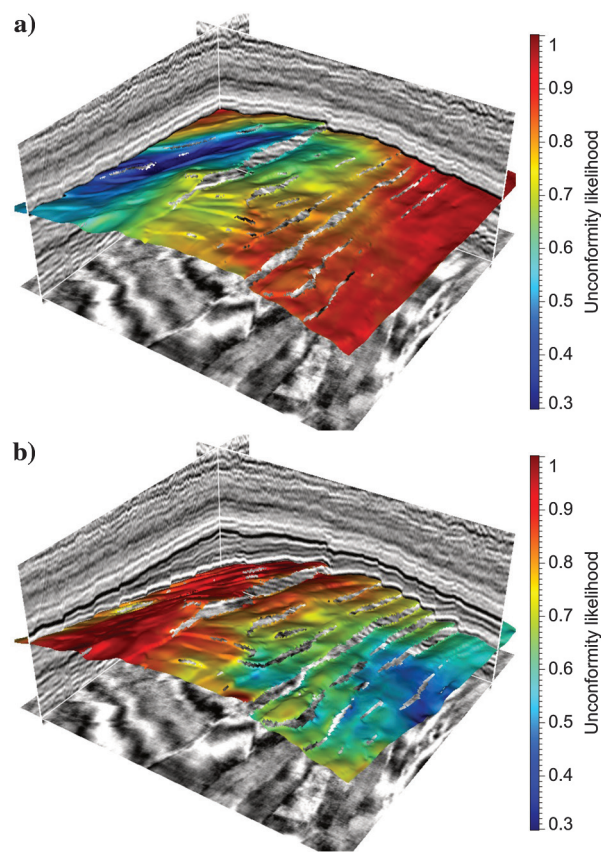
Figure 11. The two unconformity surfaces (Figure 10b and 10c) extracted in the unfaulted space are mapped back to the original space using the unfaulting shifts in Figure 7. These unconformities are difficult to directly extract from the original seismic image because they are misaligned across faults as shown in panels (a) and (b).

smoothing filter extends the structure differences, which originate within the termination areas, to the corresponding parallel unconformities and correlative conformities. In doing this, the correlative conformity and parallel unconformity are assumed to be continuous throughout the seismic image. This is why we want to first undo the faulting in the seismic image to compute an unfaulted image with continuous reflectors across faults and then attempt to extract unconformities from the unfaulted image.
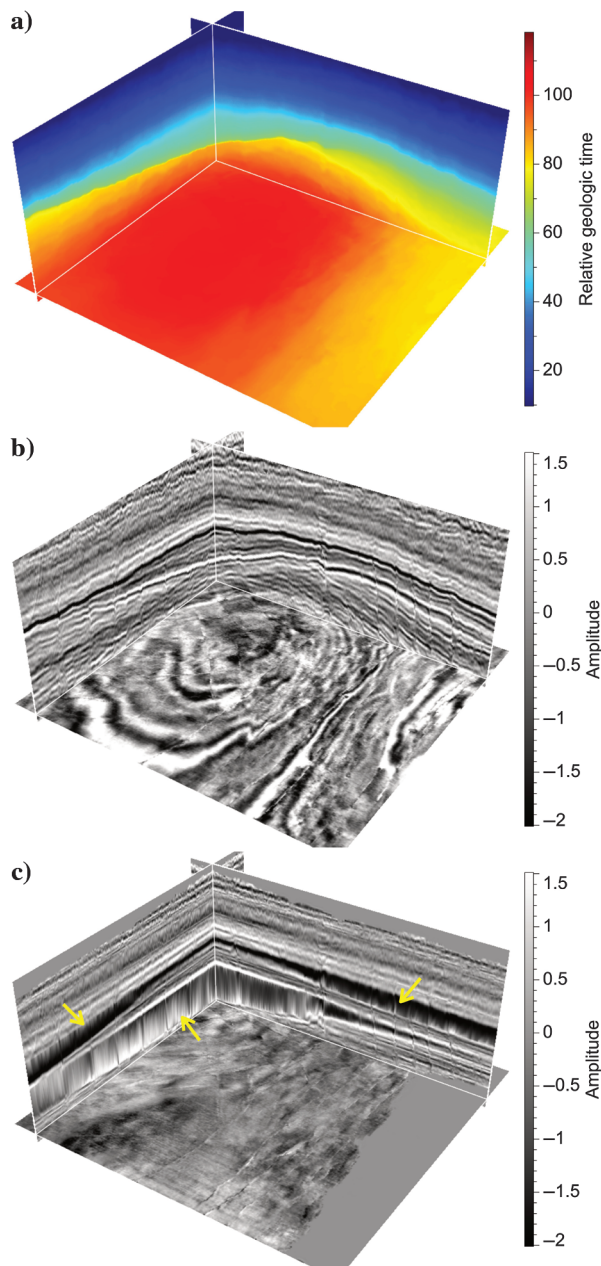
Figure 12. The unconformities (Figure 10b and 10c) are used as constraints to first compute an (a) RGT volume in the unfaulted space, and (b) the unfaulted image is then (c) flattened using the relative geologic time (RGT) volume. The vertical gaps highlighted by the yellow errors in the flattened image correspond to the two unconformities.

Figure 9 shows a synthetic example with an unconformity in the middle of the seismic image. As shown in Figure 9a, two seismic normal vector fields $\mathbf{u}_{s,c}$ (green segments) and $\mathbf{u}_{s,a}$ (yellow segments) computed from $\mathbf{T}_{s,c}$ and $\mathbf{T}_{s,a}$ are different near the termination area and its corresponding parallel unconformity. Unconformity likelihood h, defined as $h = (1 - \mathbf{u}_{s,c} \cdot \mathbf{u}_{s,a})^8$, indicates the difference of the two vector fields and therefore highlights out the termination area and its corresponding parallel unconformity as shown in Figure 9b. Figure 10a shows unconformity likelihoods computed for the unfaulted seismic image (Figure 8b). From this unconformity likelihood image, two unconformity surfaces (Figure 10b and 10c) are extracted on the ridges of the unconformity likelihoods. These two unconformity surfaces are extracted from the unfaulted image and thereby are continuous throughout the image. These two continuous unconformity surfaces can be mapped back to the original space to obtain the corresponding faulted unconformities in the original seismic image as shown in Figure 11. However, these faulted unconformmites (Figure 11) are difficult to extract directly from the original seismic image.

As an application, these extracted unconformity surfaces can be useful for estimating seismic normal vectors at unconformities with multiple-oriented seismic reflectors. A conventional structure-tensor method (Van Vliet and Verbeek, 1995; Fehmers and Höcker, 2003) can correctly estimate the normal vectors (or slopes) of the reflectors in conformable areas of a seismic image, but for an angular unconformity where two different structures meet, this method yields smoothed vectors that represent averages of orientations across the unconformity. Using the extracted unconformity surfaces as constraints for the structure-tensor method, as discussed by Wu and Hale (2015b), we are able to obtain discontinuous seismic normal vectors at unconformities, which enable us to compute a flattened image with vertical gaps corresponding to unconformities.

Flattening and horizon extraction

After fault and unconformity processing, our final step is to compute a map that flattens the unfaulted image and to extract horizons using this map. To correctly map the unfaulted image into a flattened image with vertical gaps at unconformities, we use the extracted unconformities as constraints in the flattening method as discussed by Wu and Hale (2015b).
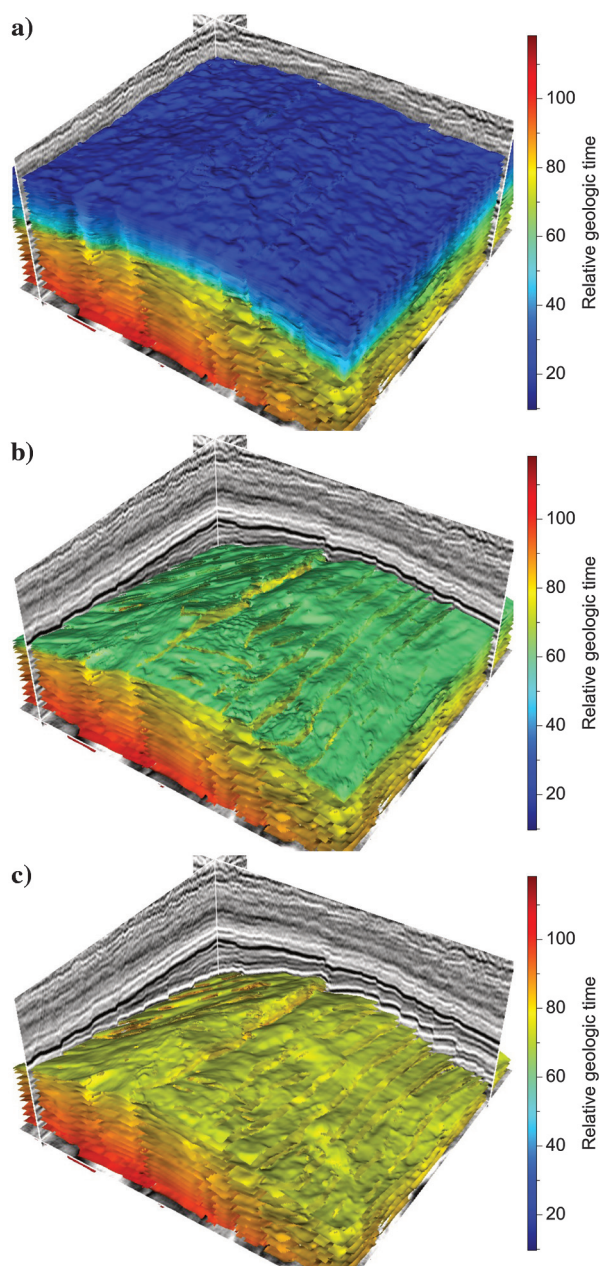
In this flattening method, we first compute vertical flattening shifts $s(\mathbf{w})$ in the unfaulted space ($\mathbf{w} = (w_1, w_2, w_3)$) by solving the following partial differential equations weighted by the unconformity likelihoods:

$$
\begin{bmatrix}
\omega \left(-\frac{\partial s}{\partial w_1} - p \frac{\partial s}{\partial w_3} \right) \\
\omega \left(-\frac{\partial s}{\partial w_2} - q \frac{\partial s}{\partial w_3} \right) \\
\epsilon_0 (1 - \omega) \frac{\partial s}{\partial w_3}
\end{bmatrix}
\approx
\begin{bmatrix}
\omega p \\
\omega q \\
0
\end{bmatrix}, \qquad (4)
$$

where $\omega(w_1, w_2, w_3) = 1 - h(w_1, w_2, w_3)$ and $h(w_1, w_2, w_3)$ represent unconformity likelihoods computed in the unfaulted space as shown in Figure 10a; $p(w_1, w_2, w_3)$ and $q(w_1, w_2, w_3)$ are inline and crossline reflector slopes estimated from the unfaulted seismic image $f(w_1, w_2, w_3)$ (Figure 8b); and ϵ_0 is a tiny constant number ($\epsilon_0 = 0.001$).

After computing the shifts $s(w_1, w_2, w_3)$ by solving the above equations, we then compute an RGT volume $u(w_1, w_2, w_3) = w_3 + s(w_1, w_2, w_3)$. As shown in Figure 12a, the RGT values are discontinuous at unconformities as expected because unconformities re-present hiatuses or geologic age gaps. This RGT volume $u(w_1, w_2, w_3)$ is then used to map the unfaulted image $f(w_1, w_2, w_3)$ (Figure 12b) into the flattened space to compute an unfaulted and flattened image $f(w_1, w_2, u)$ as shown in Figure 12c. In this image, all seismic reflectors are flat, and the vertical gaps highlighted by yellow arrows correspond to the two unconformities.

Horizon extraction is trivial after computing the maps of unfaulting and flattening. We first extract horizontal slices in the unfaulted and flattened space (Figure 12c). We then use the RGT volume (Figure 12a) to map these horizontal slices back to the unfaulted space (Figure 12b) and obtain curved surfaces. Finally, we use the unfaulting shifts (Figure 7) to map the curved surfaces back to the original space and eventually obtain curved and faulted surfaces, as shown in Figure 13. In this way, we can easily compute any number of seismic horizons in the original space. Figure 13 shows only three subsets of seismic horizons, which are curved and faulted.

Figure 13. Three subsets of seismic horizon surfaces that are first extracted in the unfaulted and flattened space, and then converted back to the original space using the RGT volume (Figure 12a) and unfaulting shifts (Figure 7).
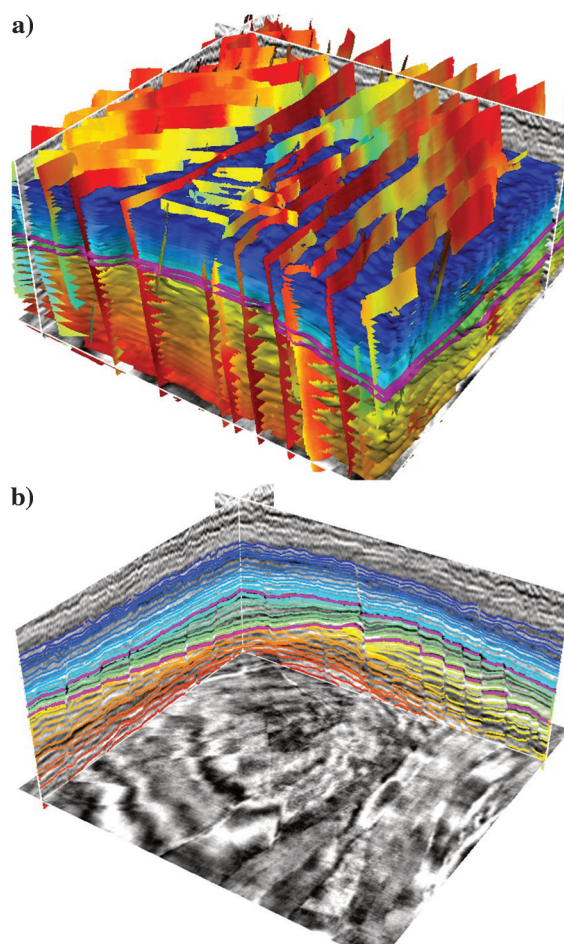
Figure 14. (a) A 3D view of the automatically extracted fault, unconformity, and horizon surfaces. The unconformities (magenta) and horizons intersect with inline and crossline seismic slices in panel (b).

Through the entire 3D seismic image processing, we obtain fault surfaces, unconformity surfaces, and horizon surfaces in the original space as shown in Figure 14a. The faults are directly extracted from the original seismic image. The unconformities (magenta surfaces) are extracted from the unfaulted seismic image and then transformed back to the original space using unfaulting shifts. The horizons are extracted from the unfaulted and flattened space and then transformed back to the original space using the RGT volume and unfaulting shifts. Figure 14b shows a different view of the unconformities and horizons, in which seismic horizons and the two unconformities (magenta curves) intersect with the two vertical seismic slices. We observe that the horizons and the two unconformities are dislocated at faults, but correctly follow seismic reflectors. We also observe that some of the horizons terminate at the two unconformities.

Conclusions

We have presented a procedure of image processing including fault processing, unconformity processing, and image flattening to automatically compute all the faults, unconformities, and horizon surfaces from a single 3D seismic image. We apply fault processing before unconformity processing and flattening because unconformities and horizons are dislocated by faults in this seismic image, and the fault processing relocates seismic reflectors across faults. We apply unconformity processing before flattening because a flattened image should be discontinuous at unconformities, and the extracted unconformities can be used as constraints to preserve the discontinuity. Moreover, the extracted unconformities can be used as constraints to more accurately estimate discontinuous seismic normal vectors near unconformities for the image flattening.

Some limitations remain in our methods. In the fault processing methods, one limitation is that we currently only estimate fault dip slips that are displacements in fault dip directions. In reality, fault slips often consist of displacements in the dip and strike directions. However, the displacements in strike directions are more difficult to estimate because they tend to be parallel to geologic layers and are difficult to resolve from a seismic image. Seismic stratigraphic features (e.g., channels) extracted from seismic horizon surfaces might be used to estimate the fault displacements in strike directions. Another limitation arises from the way we compute unfaulting shifts for the samples away from faults using simple partial differential equations. Although these simple equations can be solved efficiently and corresponding unfaulted results appear reasonable, it might be possible and preferable to use a more geologically and geomechanically correct way to compute the shifts for samples away from faults.

In computing unconformity likelihoods, one limitation is that we use vertically causal and anticausal filters to obtain structure tensors that differ at unconformities because we assume unconformities are more horizontal than vertical. This assumption is often true but is not necessary. Therefore, for future work, unconformity likelihoods might be further improved by using causal and anticausal filters that smooth in directions orthogonal to unconformities instead.

In seismic image flattening and horizon extraction, we compute only vertical shifts to flatten a seismic image and then extract horizons. However, these vertical shifts cannot flatten nonvertical deformations apparent in the seismic image. The unfaulting processing using vector shifts before flattening helps to remove some of the nonvertical deformations due to the nonvertical faults in the seismic image. However, vector flattening shifts are still preferable to better flatten an unfaulted seismic image.

After unfaulting, flattening, and extracting an entire volume of horizons, one straightforward application in the future is to use the horizons to guide interpolation of borehole data and to obtain 3D images of subsurface properties, so that the interpolated property values conform to geologic structures followed by horizons. Moreover, horizontal slices of a flattened image reveal stratigraphic features, such as channels, in 3D seismic images. Therefore, we might want to use these features to guide a sequence of 2D interpolations for horizontal slices in the flattened space, and then we map the interpolated result back to the original space to obtain a structure- and stratigraphic feature-guided interpolation.

Acknowledgments

References

Admasu, F., 2008, A stochastic method for automated matching of horizons across a fault in 3D seismic data: Ph.D. thesis, Otto-von-Guericke-Universität Magdeburg, Universitätsbibliothek.

Bahorich, M., and S. Farmer, 1995, 3-D seismic discontinuity for faults and stratigraphic features: The coherence cube: The Leading Edge, **14**, 1053–1058, doi: 10.1190/1.1437077.

Barnes, A. E., 2000, Attributes for automating seismic facies analysis: 70th Annual International Meeting, SEG, Expanded Abstracts, 553–556.

Fehmers, G. C., and C. F. Höcker, 2003, Fast structural interpretation with structure-oriented filtering: Geophysics, **68**, 1286–1293, doi: 10.1190/1.1598121.

Fomel, S., 2010, Predictive painting of 3D seismic volumes: Geophysics, **75**, no. 4, A25–A30, doi: 10.1190/1.3453847.

Gibson, D., M. Spann, J. Turner, and T. Wright, 2005, Fault surface detection in 3-D seismic data: IEEE Transactions

on Geoscience and Remote Sensing, **43**, 2094–2102, doi: 10.1109/TGRS.2005.852769.

Hale, D., 2009, Structure-oriented smoothing and semblance: CWP Report 635.

Hale, D., 2013a, Dynamic warping of seismic images: Geophysics, **78**, no. 2, S105–S115, doi: 10.1190/geo2012-0327.1.

Hale, D., 2013b, Methods to compute fault images, extract fault surfaces, and estimate fault throws from 3D seismic images: Geophysics, **78**, no. 2, O33–O43, doi: 10.1190/geo2012-0331.1.

Hoek, T. V., S. Gesbert, and J. Pickens, 2010, Geometric attributes for seismic stratigraphic interpretation: The Leading Edge, **29**, 1056–1065, doi: 10.1190/1.3485766.

Lomask, J., A. Guitton, S. Fomel, J. Claerbout, and A. A. Valenciano, 2006, Flattening without picking: Geophysics, **71**, no. 4, P13–P20, doi: 10.1190/1.2210848.

Luo, S., and D. Hale, 2013, Unfaulting and unfolding 3D seismic images: Geophysics, **78**, no. 4, O45–O56, doi: 10.1190/geo2012-0350.1.

Marfurt, K. J., R. L. Kirlin, S. L. Farmer, and M. S. Bahorich, 1998, 3-D seismic attributes using a semblance-based coherency algorithm: Geophysics, **63**, 1150–1165, doi: 10.1190/1.1444415.

Marfurt, K. J., V. Sudhaker, A. Gersztenkorn, K. D. Crawford, and S. E. Nissen, 1999, Coherency calculations in the presence of structural dip: Geophysics, **64**, 104–111, doi: 10.1190/1.1444508.

Parks, D., 2010, Seismic image flattening as a linear inverse problem: M.S. thesis, Colorado School of Mines.

Pedersen, S. I., T. Randen, L. Sonneland, and Ø. Steen, 2002, Automatic fault extraction using artificial ants: 72nd Annual International Meeting, SEG, Expanded Abstracts, 512–515.

Pedersen, S. I., T. Skov, A. Hetlelid, P. Fayemendy, T. Randen, and L. Sønneland, 2003, New paradigm of fault interpretation: 73rd Annual International Meeting, SEG, Expanded Abstracts, 350–353.

Randen, T., S. I. Pedersen, and L. Sønneland, 2001, Automatic extraction of fault surfaces from three-dimensional seismic data: 71st Annual International Meeting, SEG, Expanded Abstracts, 551–554.

Ringdal, K., 2012, Flow-based segmentation of seismic data: M.S. thesis, University of Bergen.

Smythe, J., A. Gersztenkorn, B. Radovich, C.-F. Li, and C. Liner, 2004, Gulf of Mexico shelf framework interpretation using a bed-form attribute from spectral imaging: The Leading Edge, **23**, 921–926, doi: 10.1190/1.1803504.

Stark, T. J., 2005, Generating a seismic Wheeler volume: 75th Annual International Meeting, SEG, Expanded Abstracts, 782–785.

Van Bemmel, P. P., and R. E. Pepper, 2000, Seismic signal processing method and apparatus for generating a cube of variance values: U.S. Patent 6,151,555.

Van Vliet, L. J., and P. W. Verbeek, 1995, Estimators for orientation and anisotropy in digitized images: Proceedings of the First Annual Conference of the Advanced School for Computing and Imaging, ASCI'95, ASCI, 442–450.

Wei, K., 2009, 3D fast fault restoration: U.S. Patent 7,480,205.

Wei, K., and R. Maset, 2005, Fast faulting reversal-draft version 3: 75th Annual International Meeting, SEG, Expanded Abstracts, 771–774.

Wu, X., and D. Hale, 2015a, 3D seismic image processing for faults: 85th Annual International Meeting, SEG, Expanded Abstracts, 1728–1733.

Wu, X., and D. Hale, 2015b, 3D seismic image processing for unconformities: Geophysics, **80**, no. 2, IM35–IM44, doi: 10.1190/geo2014-0323.1.

Wu, X., and D. Hale, 2015c, Horizon volumes with interpreted constraints: Geophysics, **80**, no. 2, IM21–IM33, doi: 10.1190/geo2014-0212.1.

Wu, X., S. Luo, and D. Hale, 2015, Moving faults while unfaulting 3D seismic images: 85th Annual International Meeting, SEG, Expanded Abstracts, 1692–1697.

Wu, X., and G. Zhong, 2012, Generating a relative geologic time volume by 3D graph-cut phase unwrapping method with horizon and unconformity constraints: Geophysics, **77**, no. 4, O21–O34, doi: 10.1190/geo2011-0351.1.

Xinming Wu received an engineering degree (2009) in geophysics from Central South University, an M.Sc. (2012) in geophysics from Tongji University, and a Ph.D. (2016) in geophysics from the Colorado School of Mines where he was a member of the Center for Wave Phenomena. He worked at Transform Software and Services/DrillingInfo during the summer and winter of 2014 as an intern. Since 2015, he has been working at Bureau of Economic Geology, University of Texas at Austin, as a visiting scholar and postdoctoral fellow.

Dave Hale received a B.S. (1977) in physics from Texas A&M University and a Ph.D. (1983) in geophysics from Stanford University. He has worked as a field seismologist and research geophysicist for Western Geophysical, as a senior research geophysicist for Chevron, as an associate professor at the Colorado School of Mines, as a chief geophysicist and software developer for Advance Geophysical, and as a senior research fellow for Landmark Graphics. In 2005, he returned to the Colorado School of Mines as the C. H. Green Professor of Exploration Geophysics.